Watching soot inception via online Raman spectroscopy

Kim Cuong Le, Christophe Lefumeux, Thomas Pino

Title: Watching soot inception via online Raman spectroscopy

Authors: Kim Cuong Le[1,2*], Christophe Lefumeux[1], Thomas Pino[1]

Affiliations:

1. Institut des Sciences Moléculaires d'Orsay (ISMO), CNRS, Univ Paris Sud, Université Paris-Saclay, F-91405 Orsay, France

2. Present address: Division of Combustion Physics, Department of Physics, Lund University, P.O. Box 118, SE-22100 Lund, Sweden

Corresponding author

Kim Cuong Le,
Email: thi_kim.cuong_le@forbrf.lth.se
Phone: +46 46-222 93 60, Sweden

Abstract: In this work, online spontaneous Raman spectroscopy was applied to study the soot inception and growth zones of a low pressure premixed ethylene/oxygen flame. Firstly, we measured online Raman spectrum of aerosol soot extracted from the flame. The spectrum was compared to ex situ Raman measurements of the same soot after being deposited on a window. In the aerosol soot particles, the presence of an abundant sp hybridized carbon chain component is inferred accompanying a polycyclic aromatic component. Both cumulenic and polyynic chains are affected by the deposition under vacuum and by the pressure as it is raised to atmospheric, revealing that the sp phase is no longer visible in the ex situ characterization of the sampled soot. Secondly, we monitored the Raman spectra of aerosol soot as a function of the height above the burner. Comparing spectral differences of by-products along the blue to orange zone of the flame permitted the soot formation and evolution to be probed. The online spectra, by avoiding structural modifications of the real soot structures by deposition, highlight the role of unsaturated carbon chains in the chemical condensation scenario.

Keywords

Online Raman spectroscopy, soot, soot evolution, inception, maturity

1. Introduction

Adverse impacts of black carbon on climate change and human health are often pointed out as pertinent issues in almost all environment and health studies [1,2]. It is therefore a central motivation of many studies to focus on their formation in natural and artificial burning processes as well as on their emission in the atmosphere. The scientific interest for soot formation processes is to develope more efficient and less polluting combustion techniques and to produce on a large scale and cheap nanomaterials with a variety of chemical properties in both science and industry; for instance carbon fullerenes and carbon nanotubes [3,4] or graphene and graphene-like materials [5,6]. Although soot formation occurs within few milliseconds to reach particle diameters of 30 nm [7], the whole process is extremely complicated, including three main stages: soot precursor formation, soot particle evolution and the soot inception between them [8–10].

Five decades ago, our knowledge on soot formation was limited to empirical and phenomenological observations. The central role of acetylene and condensed polycyclic aromatic hydrocarbons (PAHs) in soot formation was only recognized in the mid 1980s with the pioneering study of Frenklach and coworkers [11]. They are widely accepted nowadays in the combustion community as the building blocks in soot particle formation [10,12–14]. Concomitantly with numerical simulations, experimental techniques have been developed in order to investigate soot formation in combustion processes [15–19]. In spite of significant advances achieved in experimental optical diagnostics and modelling studies on soot formation, there are still deficiencies in our understanding of particle formation and evolution during combustion [20]. The crucial step from the molecular phase to incipient soot particles remains yet unattained to allow fruitful determination of the gradual transformation of the first soot particles [10].

Ex-situ Raman spectroscopy is a powerful tool to investigate carbonaceous matter because it is nondestructive and very sensitive to graphitic structures [21–24]. However, sampling and deposition may cause significant pertubations to the soot particles [20], their structures are thus expected to be changed during sampling. Recently, via online Raman spectroscopy, we investigated soot in the aerosol phase. We have shown that soot particles exhibit highly disordered structures and an abundant sp hybridization component beside of the expected sp^2 carbon content [25], an observation lacking in ex situ measurements of deposited soot [22,23,26–29]. Online spectra involving Raman scattering and photoluminescence (PL) signals were shown to provide crucial spectroscopic information to advance out understanding of the evolution of soot along the flame. This technique successfully complements combustion diagnostics besides other laser diagnostics, for instance laser induced

incandescence (LII), laser induced fluorescence (LIF), light extinction, elastic light scattering and cavity ring-down spectroscopy.

The objective of this study is to explore the structural transformation of the soot particles along the flame, with a particular attention on the inception zone. The nanostructure of soot particles in the aerosol phase at a specific height above the burner (HAB) was first compared to the soot nanostructure after deposition. We then monitored online the Raman scattering spectra of aerosol soot sampled in a premixed low pressure flame to investigate the pristine soot nanostructure directly in the aerosol phase, without the bias of sampling on a substrate. It should be stated that "online" and "ex situ" measurements are used for aerosol soot and deposited soot, respectively. After description of the experimental conditions, the results and the analysis procedure are presented. The discussion section then exploits spectral indices to consider the role of carbon chains in the soot formation and evolution.

2. Experiment

The flame apparatus and the optical components for online Raman measurements are similar to the previous work [25]. However, the quartz cone has been replaced by a new one with a smaller diameter hole (1 mm). A schematic drawing of the experiment in the Nanograins chamber is shown in Fig. S1 in the Supplementary Materials. In addition, the flame conditions in this study are also different from the flames published in 2019 [25]. Briefly, ethylene (C_2H_4) premixed with O_2 at an equivalence ratio $\Phi = 3.15$ (or C/O ratio equal to 1.05) flows through a 60 mm diameter McKenna burner at a rate of 4 $sl.min^{-1}$ in a combustion chamber maintained at 4 kPa. The adiabatic temperature of this flame is predicted to be about 2150 K and the flame height observe to be about 6 cm. This particular flame was chosen because we thoroughly investigated (ex situ) the soot particles sampled at different HAB as laboratory analogues of interstellar dust via infrared to vacuum ultra-violet spectroscopies [30]. N_2 gas shield around the burning region was applied at a controlled flow rate of 3 $sl.min^{-1}$. The quartz cone was inserted into the flame to extract gas and soot particles that then expanded into a monitoring chamber through a Laval nozzle, shaping a flow at 0.01 kPa. Argon was injected (0.5 sl min^{-1}) into the region between the cone and the Laval nozzle throat to control the molecular flow that partially focuses the particles on the flow axis and to cool the extracted flame products down to room temperature. It should be noted that probe clogging due to soot deposition was not an issue in the present condition because of the low pressure and the explored HAB limited to 30 mm or below. However, introducing the cone is known to perturb the structure of the flame due to influence on the thermal balance and flow field [31]. The spatial resolution for the HAB is expected to be about 2 mm or slightly less.

The excitation laser was a vertically polarized continuous laser (Verdi, Coherent) firing at 532 nm and operating up to 5W in a counter-propagating direction to the soot beam. Although the beam was focused and laser irradiance was about 50 kW/cm^2 at the focused point, the particles experience the CW laser beam during only few hundreds of microseconds while flowing. This value is far below that of conventional measurements on sampled soot on a substrate using a Raman microscope (seconds or minutes). As a consequence, no laser heating is expected to modify the particle structures, as revealed via the similarity of the spectral profiles at various laser irradiances in Fig. S2.

An optical device for collecting the scattered and emitted light was developed and integrated into the Nanograins monitoring chamber. Scattered light was collected at a 90^o configuration by an achromatic spherical lens L_1 (f_1 = 50 mm). The collimated light was then focused on a fiber optical bundle by a second achromatic spherical lens L_2 (f_2 = 125 mm) to adapt the light beam to the numerical aperture of the fiber optical bundle. Then, the signal is guided to the spectrometer. It should be noted that a third short focus cylindrical lens L3 (f_3 = 20 mm) was inserted to (roughly) compensate the extended size of the source due to the overlap between the laser and molecular beam along the propagation axis. The collected light passed through the round-to-linear optical fiber bundle before entering a spectrometer (model Acton SP 2300, Princeton Instruments) coupled with a CCD camera (PIXIS 400, Princeton Inst.). In order to observe the large spectral region including Raman signals and PL, a grating with 300 grooves/mm and 500 nm blaze wavelength was used. Note that a StopLine notch filter and a Razor-Edge (high-pass) filter were inserted in front of the entrance of the fiber bundle and the spectrometer to cut off the elastic scattering at 532 nm. Only for polarization study, a polarizer was inserted after the filters. For the parallel (p) polarization configuration discussed in this work, the polarization axis of the polarizer is parallel with the electric field vector of the incident light, whereas for the perpendicular (s) configuration, the polarization axis of the polarizer is orthogonal to the electric field vector of the incident light. The spectral resolution was 50 cm^{-1}. For spectral intensity correction, we used a calibrated blackbody light source to achieve spectral response of the fiber-coupled the spectrometer.

Two sets of experiments were performed. One set was performed to compare the aerosol soot and the deposited soot Raman spectra, fixing the HAB at 18 mm. The second set was devoted to online detection of the Raman scattering of the aerosol soot particles, after extraction at different flam heights. For the first set of experiments, the online Raman spectrum was performed in the aerosol phase, within the molecular flow. Then an optical silicate window was inserted in the molecular flow during 45 min to obtain a few-micron thick film of soot. The Raman spectrum of the soot film was monitored immediately after deposition under vacuum at a pressure of 0.002 kPa. After that, the film was then extracted through our window insertion chamber, allowing to maintain the monitoring

chamber under vacuum, and subsequently stored under atmospheric conditions for several days before ex situ Raman measurement. The ex situ Raman spectrum at atmospheric pressure was characterized using a commercial Renishaw Raman spectrometer at 514 nm with a 4 cm^{-1} spectral resolution.

Each Raman spectrum of aerosol soot was obtained using a laser irradiance of about 50 kW/cm^2 with spectrum acquisition time of 900 seconds while that of the soot film using the same optical configuration was 4 kW/cm^2 and 500 seconds, respectively, in order to achieve a sufficient signal to noise ratio and so to measure the spectra at several HAB within the same set of experiments. As short an exposure time as possible was important to achieve in order to ensure reproducibility by enabling the comparison of several spectra between sets of experiments. The irradiance values are typical for Raman measurements and do not lead to laser heating. In particular, for the aerosol phase, the flow conditions reduce the interaction time of laser and aerosol soot particles below 1 ms, such that no laser heating is expected [18]. In Fig. S2, a survey of the excitation irradiance dependence of online spectra of soot was made for HAB = 20 mm, in which the excitation irradiance was increased from 0.1 to 50 kW/cm^2. No modifications can be detected in soot structures as indicated by the stable spectral profiles. Online Raman measurement is a very challenging experiment since the Raman signal of the aerosol phase is orders of magnitude weaker than that of deposited soot. The clear advantage of the online configuration is to avoid the luminous flame background.

3. Results

3.1 Raman spectra of aerosol and deposited soot

Figure 1 shows Raman spectra of aerosol and deposited soot particles extracted at a HAB of 18 mm, at the rim between the oxidation zone and the soot growth yellowish zone (therefore at a temperature close to the maximum of this flame). Figure 1A shows the raw spectra while in Fig.1B the spectra are plotted after subtraction of the fluorescence backgrounds, and normalized to the maximum of the band at about 1600 cm^{-1}. The fluorescence subtraction will be detailed in section 4. In the aerosol phase, the PL is probably dominated by the molecular component (mainly free-flying PAHs [18]) and decreases in intensity with Stokes shift. In the deposited phase the PL probably arises from PAHs adsorbed on the soot particles with the maximum appearing shifted to longer wavelength, as is usually observed using an excitation at 532 or 514 nm [14], [15], [19]–[21]. It should be noted that the intensities of the bands observed in the spectral region between 1700 – 2300 cm^{-1} are clearly weaker in the Raman spectra of the deposited soot. A more in-depth analysis will be presented in the spectral analysis section.

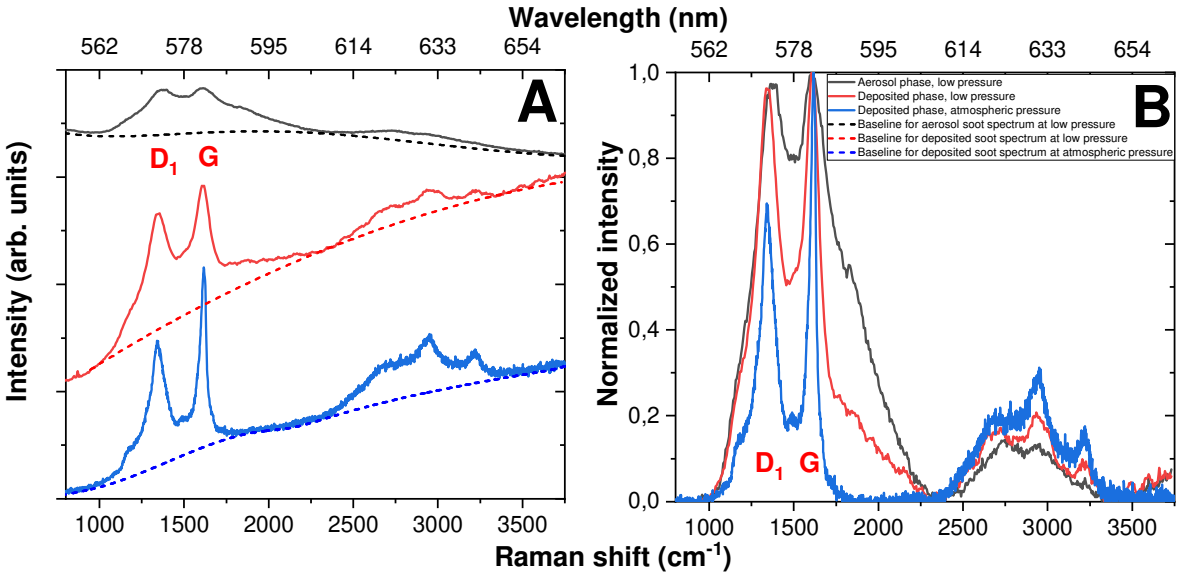

Figure 1: Raman spectra of soot produced by the same ethylene/oxygen flame conditions (C/O = 1.05, P = 4 kPa, HAB = 18 mm) in the aerosol phase at low pressure (black curve), deposited phase under vacuum (red curve) and deposited phase at atmospheric pressure (blue curve). (A) Raw data, (B) Raman spectra after subtraction of the fluorescence background, their relative intensity being scaled to the maximum at about 1600 cm^{-1} Raman shift.

Polarized light in Raman spectroscopy is very useful to probe information of molecular orientation and symmetry of the bond vibrations. Polarization effect can also be applied for crystalline and highly structured materials where symmetry is evident. For disordered structure such as deposited soot from the flames, their Raman signal is unpolarized [32]. We have applied this study to explore polarization sensitive vibrational modes, i.e. the symmetric ones that could be only observed from free-flying molecules. In Fig. 2, the Raman scattered signals in two configurations have the same in shape. Only their absolute intensities are slightly changed due to the diffrent transmission of the polarizer as a function of the angle between their polarizing axes. It should be noted that the fiber optical bundle is not polarization maintaining and the overal response of the optics and spectrometer were checked for both polarization configurations and were found not sensitive to it.

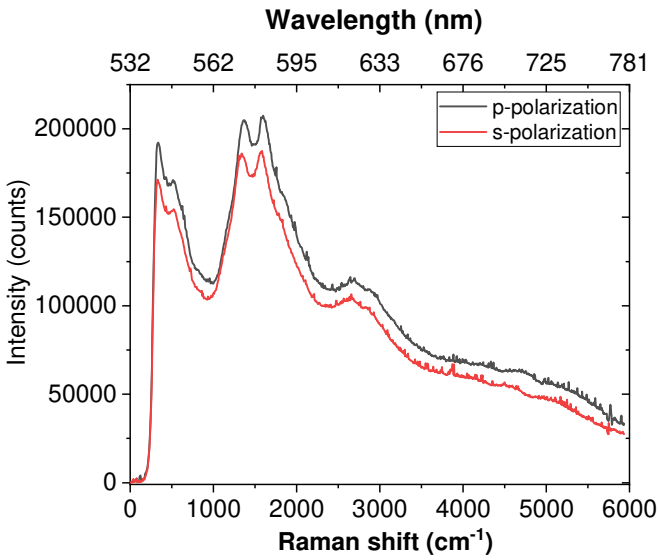

Figure 2: Online spectrum of soot produced at HAB = 18 mm in parallel (black curve) and perpendicular (red curve) polarization geometries.

3.2 Online Raman spectra across soot inception and growth zone

Figure 3 shows online emission and scattered spectra of aerosol soot produced along this C_2H_4 / O_2 flame as a function of the Stokes shift. The soot spectra are vertically translated in the figure following the order of the HAB sample distances. All are monitored with the same conditions, such as laser power and acquisition time, thus relative intensities are real.

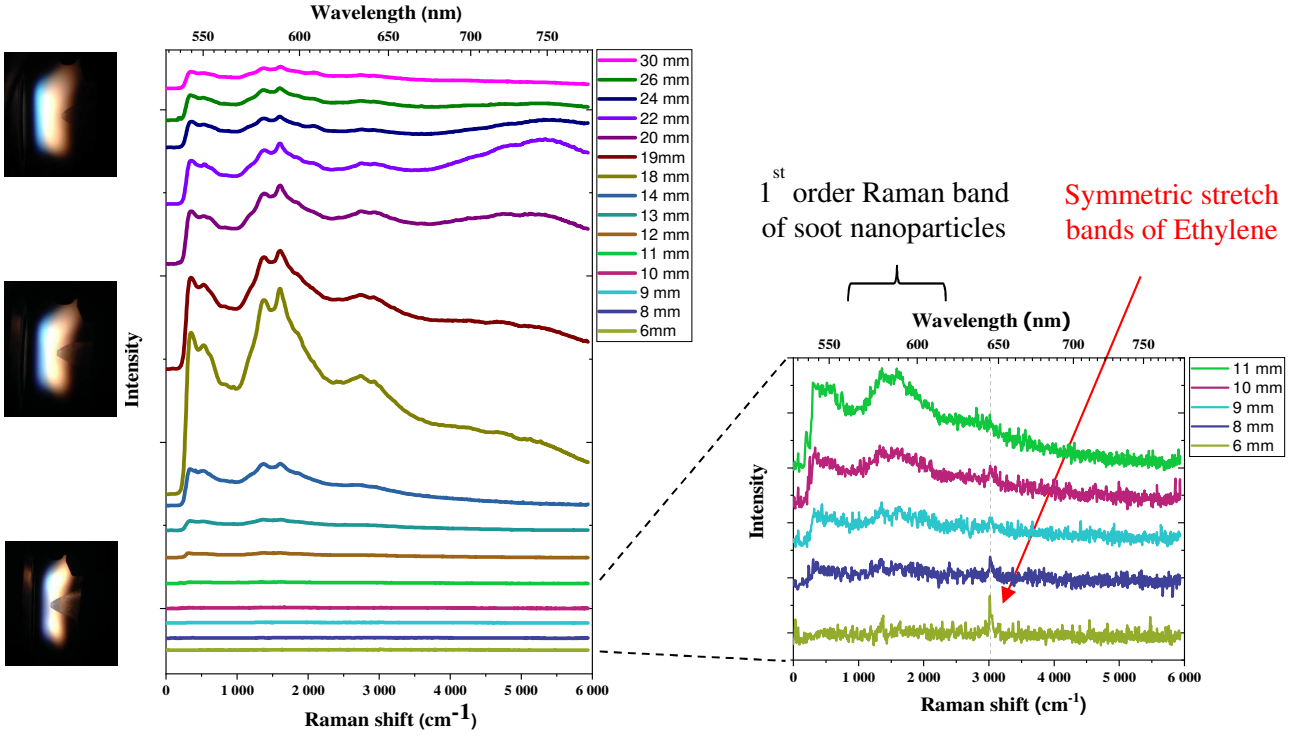

Figure 3. The soot produced along the flame is investigated by online Raman spectroscopy. On the left, from the bottom to the top, the photos of the cone inserted into the flame at 14, 22, 30 mm of height above the burner (HAB). Intensities are as measured and comparable (see text for details). On the right, vertical zoom spectra at small HAB, within the inferred inception zone.

There are several remarkable points in these spectra. The first one, specified in Fig. 4A, is the appearance of Raman symmetric stretching band (C-H stretch) of ethylene (the fuel) at 3025 cm^{-1} whose intensity decreases as the HAB is increased from 6 mm to 11 mm. At 12 mm HAB, this signal is no longer detected. Simultaneously, the clear appearance of a Raman signal showing bands whose characteristics are close to the D_1 and G bands, the two predominant Raman modes of carbonaceous particles in the first order band spectral region, at ~ 1350 cm^{-1} and ~1610 cm^{-1}, respectively [22,23,26]. At 8 mm, while possible contribution of gas phase molecular species cannot be eliminated, the Raman bands are probably those of the incipient and/or the first soot particles formed in the flame. The clearer spectral features can be seen in Fig. S4 in the supplementary. The second point is the appearance of shoulder peaks at approximately 1800 and 2100 cm^{-1} highlighted by grey columns in Fig. 4B. The third point is a broadband visible emission at 750 nm which builds up, then reduces and red shifts when the HAB increases. This broad emission band appears clearly in the spectra at HAB from 18 to 30 mm as shown in Fig. 4C.

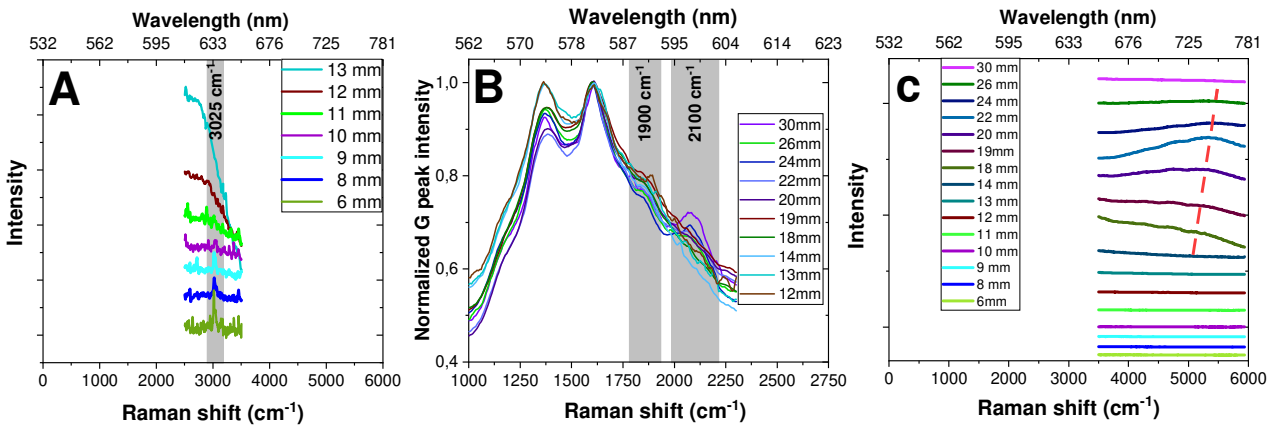

Figure 4

Three remarkable spectral regions in online spectra: A. Raman finger print of the ethylene fuel in the flame visible in the grey marked region. B. Zoom of the online spectra in the first order Raman spectral region, intensities are normalized to that of the G peak. The appearance of two peaks at about 1900 cm^{-1} and 2100 cm^{-1} is highlighted by the grey bands. C. The evolution and red-shift of a broadband visible emission at 750 nm

4. Spectral analysis

4.1. Fluorescence subtraction

In each spectrum, the Raman signal is superimposed on a PL background. The PL is mostly due to organic compounds including PAH formed during the combustion process [33,34]. Generally, we do not know the PL spectra of the products extracted from our flame. However, we know that PL is expected from the population of organic compounds including PAHs that should present in the flame by-products [35]. Regarding the strength of the signal, it is clear that this PL is very weak because it does not overwhelm the Raman signal. In addition, it has been shown that the shape of this PL may not change much with HAB [35].

One key step in the data treatment is to obtain pure Raman signals of soot from these spectra, i.e. to remove the emission contribution *without additional information.* The procedure for PL background subtraction step starts from the normalized spectra in Fig. 5A. Each spectrum consists of the first and the second-order spectral region of the Raman signals spread from 920 to 3700 cm^{-1} superimposed on the contribution of PL. The first PL component is underneath the Raman signal. The second PL component is the broadband visible emission whose peak position is at about 750 nm. It should be noted that the second PL component only appears in spectra at HAB higher than 14 mm.

At HAB $\leq$14 mm, the PL signals are quite similar. The spectral region from 920 cm^{-1} to 3700 cm^{-1} consists of Raman and PL contributions. Therefore, a second order polynomial function was used between three points whose abscissas are 920, 2350 and 3700 cm^{-1} on the spectrum and enabled to extract the Raman signal of soot. In the spectral regions below 920 cm^{-1} and above 3700 cm^{-1}, there is only PL contribution. The representative PL subtraction of soot spectra is plotted in Fig. 5B and 5C.

The PL component at HAB = 14 mm is used as a reference for the 1st PL component. At HAB above 14 mm, spectra consist of soot Raman bands, the 1st PL and the 2nd PL components. The 1st PL component fit at a certain HAB is achieved by scaling the reference at 920 cm^{-1}. After that the Raman signal and the 2nd PL signal are separated by a second order polynomial function. This step is visualized in Fig. 5D. It should be emphasized that the 2nd PL appears mostly at a Stokes shift above 4000 cm^{-1} where a very weak contribution of the 1st PL is found.

In summary, we can separate each spectrum into three components: the 1st PL considered as the background, the broadband red emission (called the 2nd PL) and the appearance of Raman spectra of soot particles containing the first and second order Raman scattering.

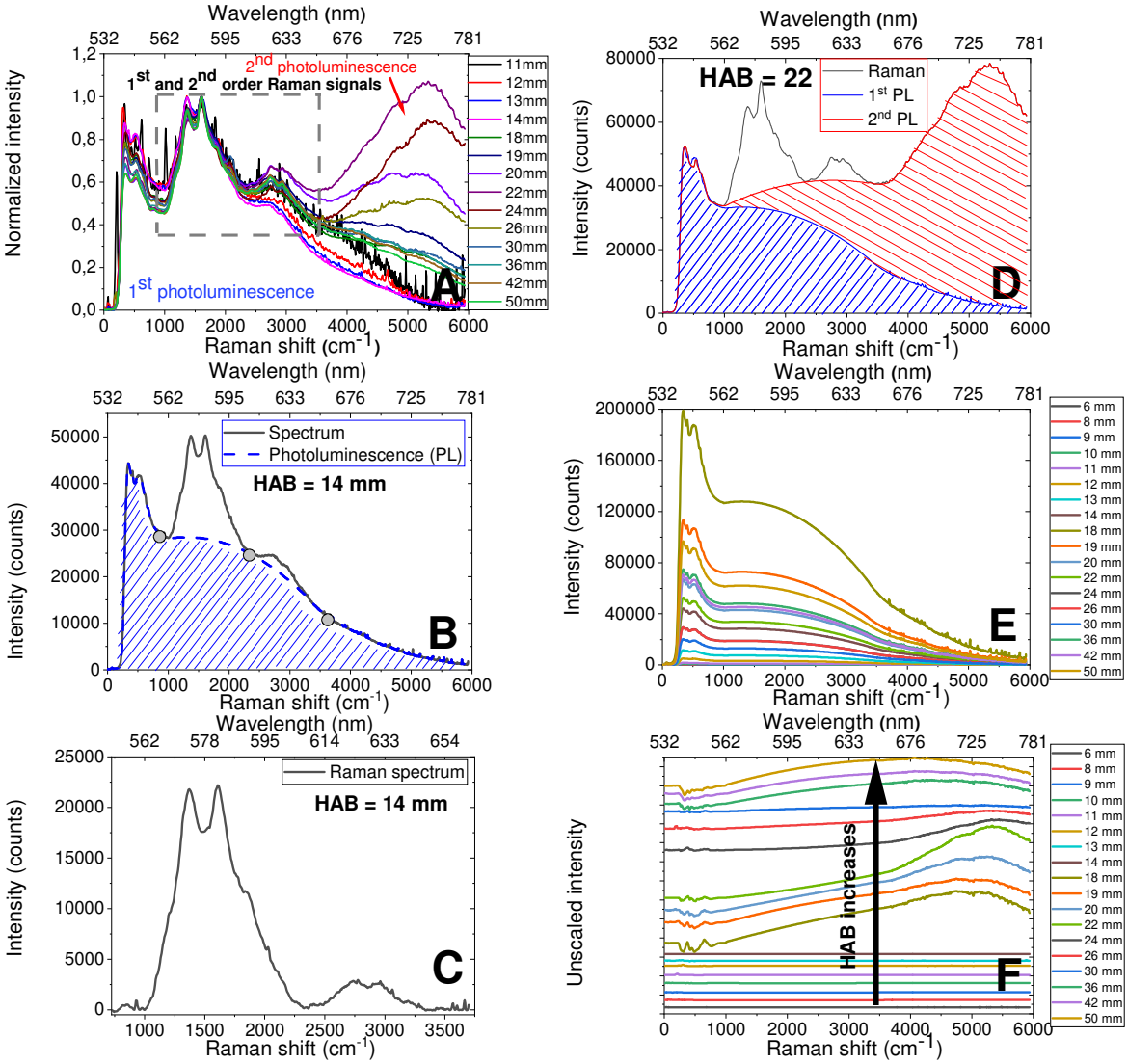

Figure 5

Subtraction of photoluminescence (PL) and Raman scattering signals in online spectra of soot

A. Normalized online spectra of soot at HAB = 11 mm to HAB = 30 mm (HAB < 11 mm is not plotted because their S/N are very low).
B. Photoluminescence and Raman signals in spectra at HAB = 14 mm. A second order polynomial function was applied beneath the spectral region 900 to 3500 cm^{-1} where the first-order and second-order Raman scattering appear. The blue striped area is the PL signal.
C. Raman spectrum of soot at HAB = 14 mm after PL subtraction.
D. Photoluminescence and Raman signals in the spectra of soot at HAB = 22 mm. A second order polynomial function was applied beneath the spectral region 900 to 3500 cm^{-1} where the first-order and second-order Raman scattering appear. The PL is then separared into two components. The blue striped area is the 1st PL appearing at all HAB. The red striped area is the 2nd PL appearing when HAB is above 14 mm. The green curve superimposed on PL is the Raman signal.
E. The evolution of the 1st PL of soot at all HAB.
F. The evolution of the 2nd PL of soot at all HAB. The unscaled spectra are vertically translated for easier observation of the peak position.

4.2 Spectral fitting and band analysis

Compared to Raman spectra of deposited soot in the literature [22,23,27], the D_1 and G bands of soot in the aerosol phase are much broader and spectral congestion is evident. Many band combinations for curve fitting were applied to reach a consistent characterization of soot particles from spectral indices. At low HAB, there is a contribution of ethylene Raman signals in Raman spectra of soot and/or soot precursors as plotted in Fig. 6A and Fig. 6B. At high HAB, the first-order Raman bands can be well-fitted by a combination of five Gaussian peaks (D_4, D_1, G, C_1, C_2) and the second-order Raman bands require a combination of four Gaussian peaks ($2D_4$, D_4+D_1, D_1+G, $2D_2$) as we can see in Fig. 6C. More details of the fitting model are given in Fig. S3, Fig. S4, and Note S1. The spectral parameters are summarized in Table S1. It is noteworthy that the same band fitting procedure was used for both online and deposited soot.

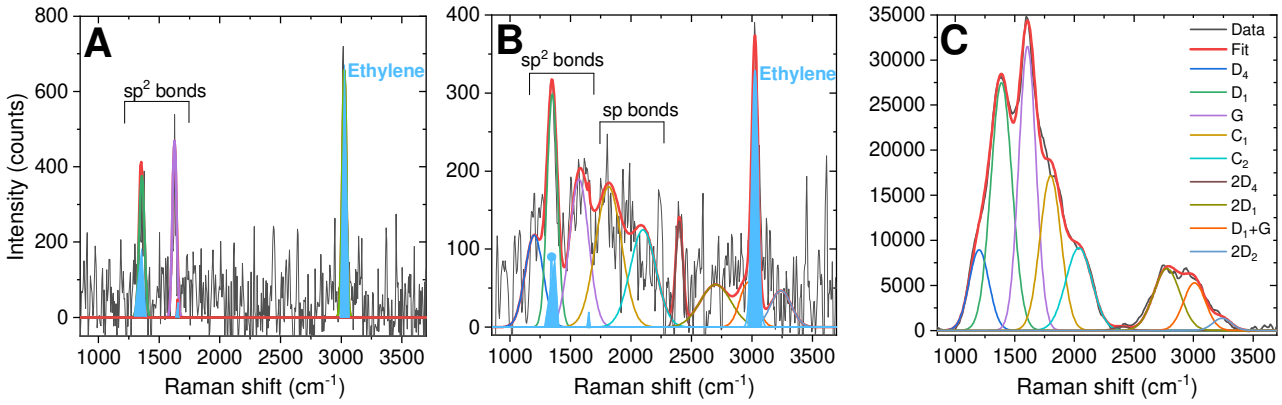

Figure 6. Deconvolution of Raman spectrum of aerosol soot produced at (A) HAB = 6 mm (B) HAB = 8 mm, and (C) HAB = 22 mm. The experimental data is the black line. The result of the best fit is plotted with the solid red line. The ethylene peaks are filled in light blue [36].

The G band involves C=C stretching motion in disordered polycyclic aromatic carbons. The D_1 peak is due to breathing mode of carbon rings and is activated in Raman spectra via the presence of defects in the graphenic structures [37]. The origin of the D_4 peak is still under debate. It may be assigned to sp^3 and sp^2 mixed carbons at the periphery of the graphenic layers, or to C–C and C=C stretching vibrations in polyene-like structures [38]. The D_2 peak indicating polycyclic aromatic units mostly at the surface of stacks should be observed as a shoulder of the G band at about 1620 cm^{-1}. However, it does not appear clearly as a separate band in our spectra and was thus not included in the deconvolution. C_1 and C_2 are representative of carbon chain structures consisting of cumulenic double-bond stretching (=C=C=) and polyynic triple-bond stretching (−C≡C−), respectively [25,33,39,40]. There is also an additional peak labelled D_3 at 1500 cm^{-1} which has often been used to evaluate the amorphous carbon fraction of deposited soot and black carbon [22]. The broadness of

the D_1 and G peaks in Raman spectra of aerosol soot precluded determination of its eventual contribution, effectively no significant improvement of the goodness of the fit is obtained by including a D_3 band. Oxygen functional groups can also contribute in the spectral region between 1700 – 1800 cm^{-1} of aerosol soot. However, this contribution is rather faint and cannot be observed after deposition and measurement at atmospheric pressure, thus oxygenated species can be excluded as a significant contribution to the spectra (and consequently to the sampled soot). Thus we do not include oxygenated chemical groups in the present study although they have been observed in some other types of soot [33,41,42]. The Raman spectra of soot also contain the second order bands in the range of about 2300 to 3300 cm^{-1}, in which two pronounced peaks at 2700 and 2900 cm^{-1} have been assigned to the $2D_1$ overtone and D_1+G combination bands [28]. The first overtone of the D_2 and D_4 modes are observed at 3240 and 2450 cm^{-1} and are labelled $2D_2$ and $2D_4$ respectively. The full width at half maximums (FWHMs) and the positions of the D_1 and G bands as well as their intensity ratios point to a highly disordered polycyclic aromatic nanostructure, i.e. poorly stacked graphenic sheets with no preferential orientation [23,24]. Using the Ferrari and Robertson [22] relation, the averaged polycyclic aromatic unit size is estimated to be about 1.2-1.5 nm as deduced from the intensity ratio between the G and D_1 bands. The evolution of all these peaks and PL was then used to build spectral indices of structural properties of soot nanostructures along the flame.

5. Discussion

5.1. Structural modification of deposited soot

As discussed above, the aerosol phase spectrum is successfully fitted by a combination of nine Gaussian bands as shown in Fig. 7A. For comparison of the spectral variation between aerosol and deposited soot, we use the same fitting procedure. The characteristics of the main Raman bands of the soot particles extracted at HAB = 18 mm are listed in Table 1.

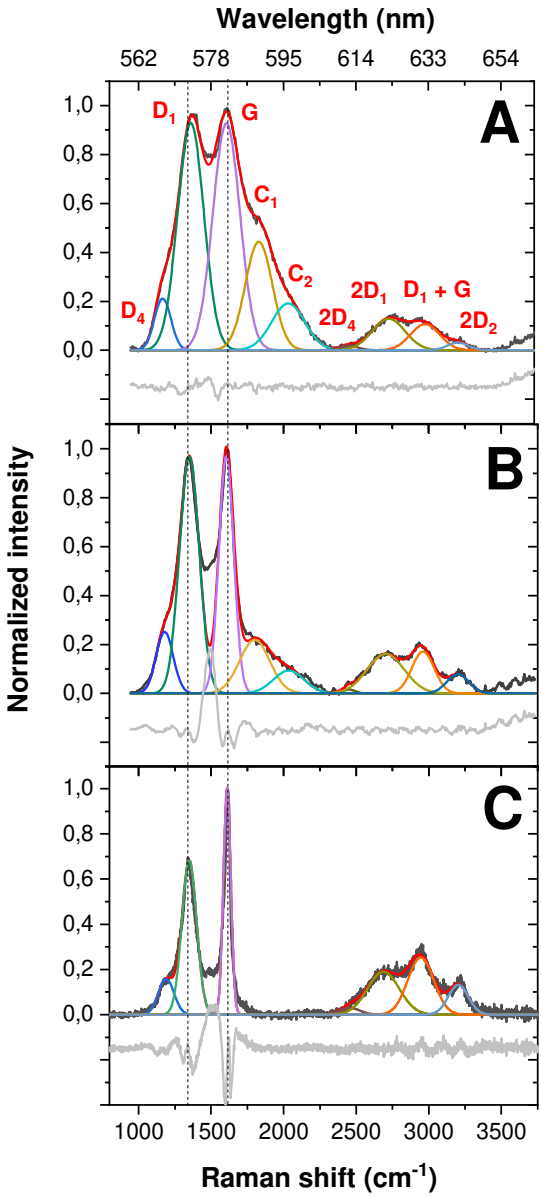

Figure 7: Decomposition of the Raman spectrum of soot (black line) in the aerosol phase (A) and deposited phases (B, C). The result of the fit is plotted with the red-line while the residual grey line (vertically shifted) shows the difference between the spectrum and the result of the fit.

It should be emphasized that spectral features of sp hybridization from aerosol phase grown nanoparticles have only been observed, to our knowledge, on aerosol soot in low pressure premixed flame [25] and carbon cluster-assembled films produced from a micro-plasma source [39,40,43,44]. To detect these, the micro-plasma formed carbonaceous particles had to be kept under vacuum and the polyynic carbon chains were shown to quickly disappear at pressures even below one atmosphere. It is noteworthy that the bands did not vary under vacuum even after several days [44]. In order to assess to the assignment of these bands to a soot component, a polarization sensitive measurement of

the Raman spectra was performed. In general, Raman spectra of gas-phase species are expected to have sharp peaks and exhibit some polarization dependences in particular for the totally symmetric vibrational modes. Such dependence is expected for the CC stretching modes in unsaturated carbon chains. Our polarization study on many different types of soot produced in various low pressure flames show no polarization effect on the sp signals [45,46]. It is also shown in Fig. 2. These results indicate the sp bonds are originated from carbon chains in the soot structure rather than gas-phase species.This highlights that the detection of the carbynoid component in the soot particles was possible thanks to the online measurement on the sampled molecular beam.

Table 1: Raman band centers ν (cm^{-1}), FWHMs (cm^{-1}), intensity normalized to that of the G band (I), and integrated intensity (Int.) as obtained from the fit. The weaker D_4 and second order bands are not listed. See text for details. Uncertainties on the positions are ± 25 cm^{-1} for aerosol and deposited soot in vacuum, and ± 10 cm^{-1} for deposited soot at atm pressure, and about 10% for the FWHMs and the integrated intensity ratios.

Raman Band	Aerosol phase (ν, FWHM, I, Int.)	Deposited phase, vacuum (ν, FWHM, I, Int.)	Deposited phase, atm. (ν, FWHM, I, Int.)
G	1612, 220, 1, 219	1610, 120, 1, 123	1610, 60, 1, 64
D_1	1360, 213, 0.96, 212	1350, 160, 0.96, 165	1349, 120, 0.69, 87
C_1	1830, 220, 0.61, 104	1800, 244, 0.22, 59	
C_2	2033, 270, 0.24, 55	2035, 250, 0.1, 26	

Interestingly, one of the main differences between the aerosol phase and deposited soot Raman spectra are the FWHMs of the D_1 and G bands. They are found to decrease when soot particles are deposited on the substrate despite being kept under vacuum (2.10^{-4} kPa). The FWHMs reduce from 213 ± 22 cm^{-1} and 220 ± 22 cm^{-1} down to 160 ± 15 cm^{-1} and 120 ± 15 cm^{-1}, respectively, but the FWHM are found to be smaller than those of amorphous carbons (~ 300 cm^{-1}) [37]. Indeed, the band's FWHM traces the degree of disorder of the samples [23]. The large FWHMs in our samples trace a high disorder and presence of defects. These contribute to the shortening of the phonon lifetime and, correspondingly, broaden the homogeneous linewidth. In addition, the large variety of local bonding induces a strong inhomogeneous broadening that lead to the mostly Gaussian profile. This indicates that the soot nanostructure is less disordered with mostly polycyclic aromatic content after deposition than that in the aerosol phase. It suggests that exposure to ambient air or atmospheric pressure leads

to additional reorganization of the soot sample. These effects clearly plead for online diagnostics of aerosol soot.

Another significant point in these measurements is the evolution of the amount of sp bonds in the soot particles upon deposition. While the FWHMs of the C_1 and C_2 bands remain similar (within the uncertainty), their Raman band intensity decreases by half after deposition. In the work of Ravagnan and co-workers, by comparing in situ NEXAFS (near-edge X-ray absorption spectroscopy) and Raman spectra of carbon cluster assembled films from a micro-plasma source, they estimated that the Raman band cross section ratio was 1.2 between the sp^2 and sp bands ($\frac{\beta_{sp^2}}{\beta_{sp}} = 1.2$) [47]. However, their value is typical of polyyne dominated structures embedded in an amorphous carbon. In the light of quantum chemical calculations on molecular cumulenic and polyynic compounds, Raman efficiencies are found to be comparable [33] albeit those of the cumulenes were shown to be sensitive to end group effects. Assuming the value is a good approximation for cumulenic structures as well, we found that in the aerosol phase the sp/sp^2 bond ratio is about 31% and this value decreases down to 25% in the soot particles after deposition and to 0% after exposure to atmospheric pressure. To clarify, the absolute value of sp/sp^2 bond ratio is determined by multiplying their integrated intensity ratio ($\frac{I_{sp}}{I_{sp^2}} = \frac{I_{C_1+C_2}}{I_{D_1+G}}$) to their Raman cross section ratio ($\frac{\beta_{sp}}{\beta_{sp^2}}$). The first value was obtained from our fitted spectra (detailed in Table 1) while the second value can be derived from Ravagna and co-workers' work mentioned above [47]. It should be noted that the broadness of the bands involving the sp bonds precludes giving an average length of the carbon chains. From the structural modification of soot after sampling processes, it is clear that online Raman spectra are mandatory to unambiguously explore low pressure flame formation and characterization of soot.

5.2 Soot formation as observed through the soot nanostructure evolution

In general, a rich laminar premixed flame can be roughly decomposed into three main observable zones: pre-reaction zone, main reaction zone and post combustion zone. The observation of the flame colors is an empirical tool that can be used to identify these different zones. The pre-reaction zone called the 'dark zone' has a typical dark bluish color. This zone is known as the 'reducing zone' and the coldest region. The reason is due to reactions of the hydrogen atom - the only abundant free radical - with fuel and oxygen impending the formation of the radical pool. The main reaction zone called the 'luminous zone' and characterized by the highest temperature starts with a green radiation because of excited C_2 molecules, then turns yellowish because of the formed soot particles. The post-combustion zone lies slightly beyond the luminous region whose temperature is still high owing to

heat emission from oxidation of CO into CO_2 [48]. This description of flame zones can also be used for our Flame 3.15. The three main zones are separated by three vertical dotted lines in Fig. 8. Obviously, the pre-reaction zone of our flame is below 6 mm of HAB while the post-combustion zone is higher 18 mm of HAB. The main reaction zone is the spatial region from 6 mm to 18 mm of HAB.

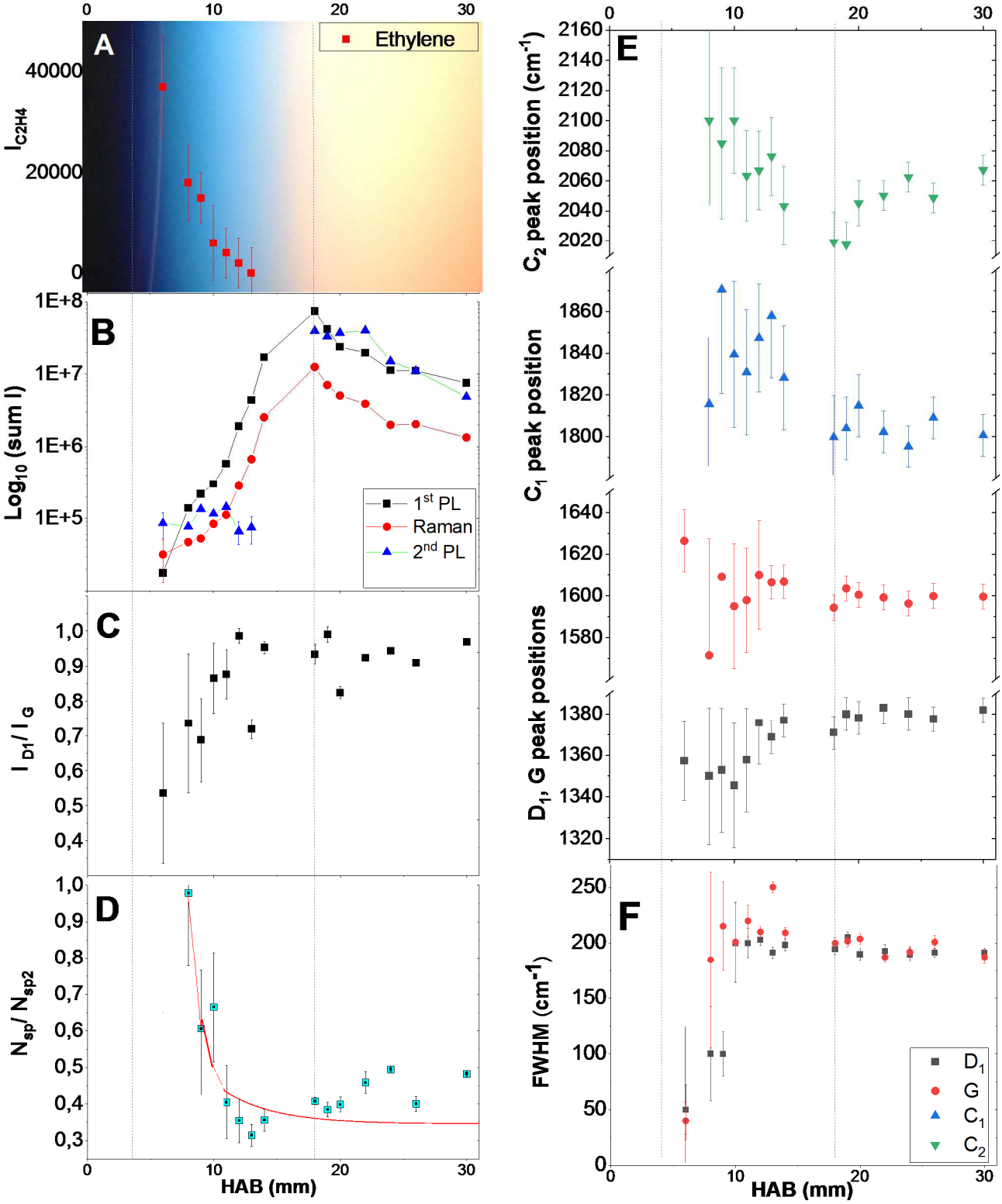

Figure 8. The evolution of soot along the flame is traced by spectral parameters. (A) integrated intensity of the ethylene signal, (B) integrated intensity of the Raman and fluorescent components in semi-logarithmic scale, (C) intensity ratio of the D_1 peak and G peak, (D) integrated intensity ratio of the sp and sp^2 bonds, (E) peak positions, and (F) full width at half maximum (FWHM) of D_1 and G versus HAB. The vertical dotted lines divide the flame into the pre-reaction zone, the main reaction zone, and the post-combustion zone (from the left to the right).

(i) Probing the inception zone: gas-to-particle conversion (6 mm – 9 mm)

In order to study the soot formation process, as revealed in Fig 8A, our investigation started at HAB = 6 mm where the transition from the dark zone to the luminous zone is observed. At this HAB, the ethylene fuel can be identified via its strongest Raman C-H stretching band at 3025 cm^{-1}, accompanied by the Raman active vibrations in the 1350 cm^{-1} and 1610 cm^{-1} regions of polycyclic aromatic structures detailed in Fig. 6A. Indeed, the Raman spectra of PAHs are characterized by few bands in approximately the same D_1 and G regions due to the similarity of their structure with graphenic islands [49]. The CH_2 bending mode at 1343 cm^{-1}, C_2 stretching mode centered at 1624 cm^{-1}, and a second overtone of CH_2 bending mode expected around 1652 cm^{-1} of ethylene should also appear in this region [36]. Their spectral contribution was determined thank to their relative peak intensity ratio with the C-H strectching mode [36]. For HAB = 8 mm, as shown in Fig. 6A and Fig. S4, the band at ~ 1350 cm^{-1} is higher than the band at ~ 1610 cm^{-1}. Stronger Raman activity of D_1 band compared to G band at HAB = 8 mm and 9 mm is expected when graphene-like PAHs grow. This is in agreement with the calculated Raman spectra for the PAHs by Negri and co-workers [49]. In addition, a significant increase of D_1 and G peak widths in Fig. 6A and Fig. 6B indicates the appearance of stacked layers or graphitic domains at HAB = 8 mm [50]. It demonstrates the collisions of probably peri condensed aromatic hydrocarbon (PCAH) resulting in turbostratic stacks of graphene sheets. The incipient particles are composed of sp^2 graphitic domain structures resembling that of PAHs bigger than pyrene [49,51].

The fuel Raman bands in Fig. 8A decline simultaneously with the emergence of additional bands in the spectral region from 1100 to 3600 cm^{-1}, shown in Fig. 8B in which a contribution of sp carbon chains is observed in the 1800-2100 cm^{-1} spectral range (Fig. 6B). At 8 mm, sp hybridized bonds are making up to approximately the same amount of sp^2 hybridized carbons (~ 50% of the total carbon content). The cumulenic bond accounts for approximately 60% of the sp hybridization. The increase of I_{D1}/I_G ratio in Fig. 8C points to a slight increase in the graphitic domain size together with a decrease of the sp carbon chain content (see Fig. 8D). This observation may address a transformation of sp carbon chains into sp^2 graphenic-sheet. Monitoring the aerosol soot Raman spectra at HAB from 6

mm to 9 mm, i.e. passing across the inception zone, thus provides new information on the nanostructures of the incipient soot particles.

The tentative scenario can be compared to that built from Desgroux et al. 2017 [31] by comparing a "nucleation" flame with a "sooting" flame. In their work, laser induced incandescence (LII) was applied across the inception zone. The inception was determined to be at the first maximum concentration of the PAH determined by ex situ time-of-flight mass spectrosmetry (TOFMS) analysis of flame products and online jet-cooled LIF, in coincidence with the appearance of the LII signal. The transition from the molecular precursors to the first particles is similar to that schemed here via the online Raman measurements. The main difference is the occurrence of sp carbon chains in low pressure ethylene flames, which could not be detected in the low pressure methane flame of the work of Desgroux et al. because the structural characterisation was performed by ex situ TOFMS diagnostics on sampled flame products. Exploration by online Raman spectroscopy of the methane flame would allow exploring the presence of sp carbon. In addition, improvement of the SNR of the Raman spectra in the 6-9 mm HAB in our flame 3.15 would be necessary to characterize more deeply the fine structures of the first particles and eventually the precursors, and comparison with other diagnostic such as online mass spectrometry of LII would bring very valuable information. Work is in progress in these directions.

In summary, the inception process of the low pressure ethylene Flame 3.15 happens within the early blue flame region at about 6 mm where the first polycyclic aromatic aliphatic mixed entities are detected. The formation of incipient soot particles at HAB = 8 mm is thus concomitant with the growth of very slightly fluorescing PAH-like structures, which may contribute to the molecular precursors for the incipient soot particles. The incipient soot particles formed undergo rapid growth by gas-to-particle conversion. They also loose hydrogen through a high-temperature carbonization process, becoming partially graphenic. The results suggest involvement of the long aliphatic carbon chains appearing and accounting for a large proportion in the formation of the incipient soot particles.

(ii) Growing process of incipient soot particles to form partially matured soot particles/young soot (9 mm – 11 mm)

For HAB up to 10 mm, the ethylene signal keeps droping (Fig. 8A) and the first PL component slightly increases (Fig. 8B). The spectrum of this PL component is comparable to that measured by laser induced fluorescence (LIF) on a premixed methane flame [35]. It was measured directly in the flame and thus on hot species while in our case all are cooled to about room temperature within the Laval nozzle flow. Considering Stokes emission spectra, our spectra show a similar trend with LIF

spectra, i.e. no noticeable variation apart from its intensity. These spectra can come from the emission of free-flying PAH. However, the use of visible wavelength excitation (532 nm) restricts the excitation to PAHs with low-lying electronic excited states. This may happen for very large sized PAHs, though they are unlikely to reach high enough abundances in flames, PAHs with defects (for instance five-membered ring) or PAH cluster derivatives [35]. Whatever the exact carrier structure, the increase of this PL feature traces the increase of PAH concentration by considering a nearly constant effect of quenching on the region of excited PAHs.

Based on liturature and our Raman knowledge on such disordered structure, we found that PAHs are distinguished from particles by the narrower sp^2 peak widths combined the stronger D_1 peak intensity compared to the G peak [45,49]. From HAB = 9 mm to HAB = 10 mm, the D_1 peak maximum intensity drops compared to the G peak maximum intensity but its FWHM increases and reaches a roughly stable value. This spectral feature addresses that the PCAH below HAB = 10 mm, potential soot precursors, are still detectable. The graphitic domains keep growing indicated by the increase of the integrated intensity ratio between D_1 and G peaks as well as the emergence of the second order of Raman spectra of soot in the range of about 2300 to 3300 cm^{-1}. The sp and sp^2 bond ratio drops down to about 40% at HAB = 11 mm, in which the polyynes are seen to be less abundant and vanish more rapidly than the cumulenes.

At the end of this stage where HAB is about 11 mm, the first and the second order Raman bands of disordered carbon materials appear more clearly. In addition, the Raman intensity increase indicates the growth in number and size of the incipient soot probably by absorbing or accreting gas phase molecules and surface growth to form young soot particles / partially matured soot particles.

(iii) The evolution process to form quasi-spherical primary particles (11 mm – 18 mm)

This region is marked by the strong increase of the intensity of the Raman spectra of the soot particles by more than 2 orders of magnitude. Nevertheless, there is also an enhancement of the first PL component in Fig. 8B. During growth process referring to coalescence, multiple first particles are loosely attached to one another to form quasi-spherical primary particles [52]. The maturation actually started after soot inception. Polycyclic aromatic unit mean size L_a (or graphitic crystallite size) grows due to dehydrogenation and aromatization of soot along the flame [53] as indicated by the increase of the intensity ratio of the D_1 and G peaks in Fig. 8C and the G peak position around 1610 cm^{-1} featuring a weak contribution of sp^2 chains. The narrowing of the G peak width starts at HAB = 13 mm and reveals graphitization in which the decrease of the interlayer spacing should also take place [52,54]. The blue shift of C_1 and C_2 bands in this flame region suggests that the carbon

chains continuously shorten [21]. The N_{sp}/N_{sp^2} decrease may point to the transformation of the sp carbon chains into sp^2 carbon bonds in graphenic sheets.

(iv) Evolution of soot toward aggregates mature soot (18 mm – 30 mm)

Raman spectral characteristics, peak positions and peak widths of D_1, G, C_1, tend to be somewhat stable. The ratio of sp hybridized bonds to sp^2 hybridized bonds is about 40%. The slight increase of N_{sp}/N_{sp2} ratio or the increase of C_1 and C_2 contribution – relative to the previous height range of HAB between 11 and 18 mm is rather attributed an insignificant trend given uncertainties at low HAB. This flame region is also characterized by the appearance of a new broad PL component centered at about 750 nm. This second PL component intensity grows up rapidly and reach a maximum value at HAB = 22 mm, then decreases. The decrease of the second PL towards the end of the flame is interpreted as decrease of the adsorbed PAHs concentration. The strong Stokes shift of this second PL points to carriers with different electronic structures than those responsible for the first PL. This new feature, unobserved until now, is tentatively assigned to the PAHs adsorbed on the soot particles and thus participating to the mass growth. The electronic structure must exhibit an optical gap below about 1.5 eV as inferred from the peak emission.

The aliphatic structures detected in our previous study [25] on soot produced by Flame 2.34 and Flame 2.46 are also detectable in this Flame 3.15. The formation of sp carbon chains seems to be a systematic characteristic of low pressure rich ethylene premixed flames. Overall, the major steps in soot formation in our premixed ethylene / oxygen flame and the respective Raman spectra can be tentatively summarized in Fig. 9.

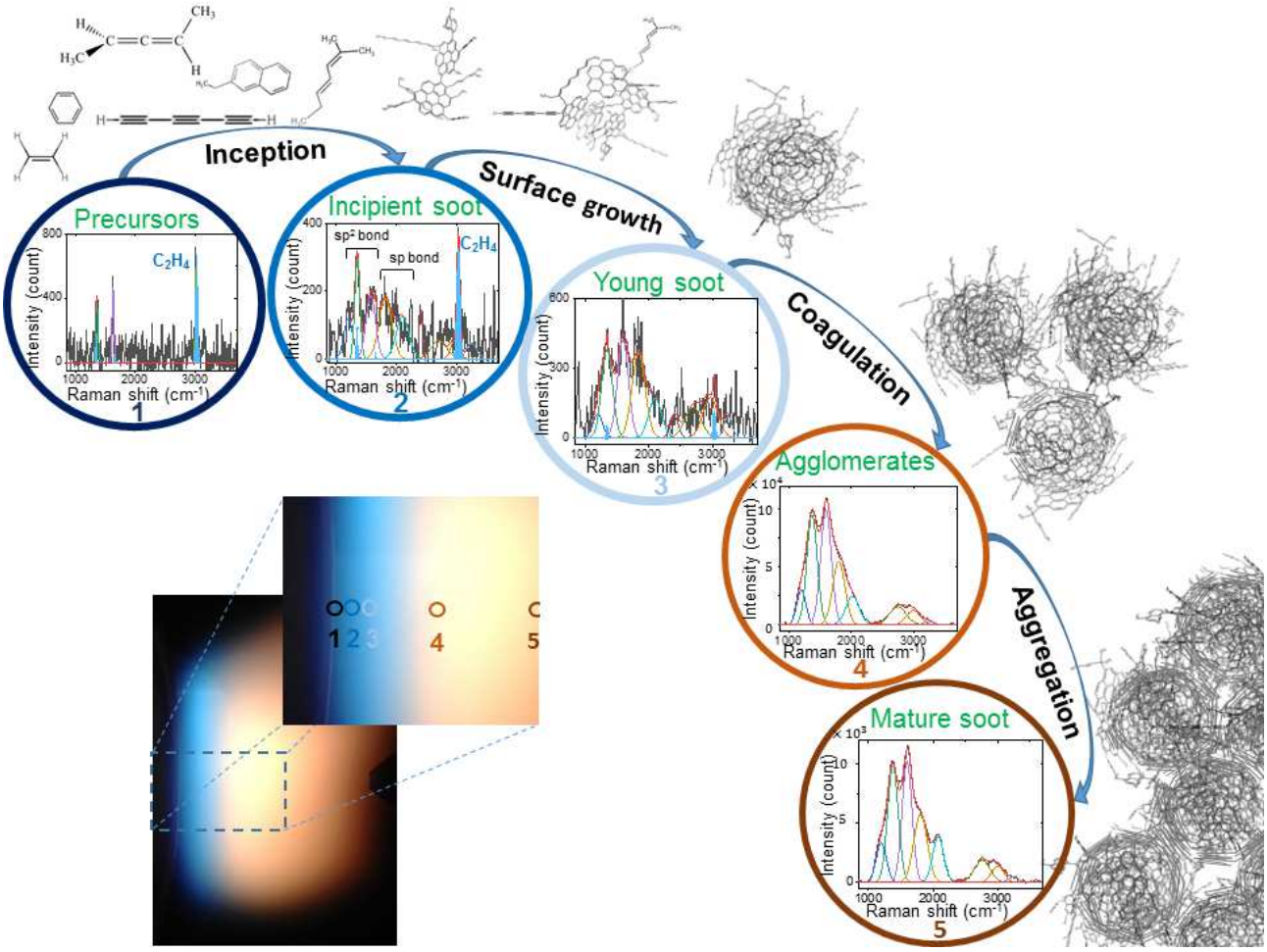

Figure 9. Schematic diagram of the major steps in soot formation and the respective Raman spectra.

6. Conclusions

For the first time, a comparison between online Raman and ex situ Raman measurements on the same soot has been carried out. Cumulenic structures have been found to dominate the sp carbon component. Both cumulenic and polyynic structures are less stable in the soot nanostructure after deposition and under atmospheric conditions. Our results reflect the influence of sampling processes on the structure characterization of soot, particularly on the sp hybridized structures and the disordered character of the sp^2 polycyclic aromatic components. This confirms the important role of online measurements in studying soot nanostructures and its formation processes.

Online Raman spectra of flame by-products have been detected within the different zones of a low pressure premixed ethylene flame. By extracting the combustion products away from the luminous flame, the weak Raman spectra of the fuel and the incipient soot particles were detected. Probably, that of the incipient soot particles can be directly monitored but with a poor signal to noise ratio. The Raman spectra reveal the nanostructures and their evolution across the inception and growth zones. Incipient soot particles are made of a large portion of sp carbon chains, above 50%, linking graphitic

domain that are probably in the size range of the soot precursors [55,56]. Subsequent growth is accompanied by reorganization of the carbon skeleton toward a higher proportion of the sp^2 aromatic carbon. The formation and growth are illustrated in Fig. 9, sketching the information learned from the first Raman spectra of incipient soot particles.

The abundant component of sp hybridized structure in soot produced by the low pressure combustion conditions suggests that polycyclic aromatic molecules as well as carbon chains are involved in soot formation in such flames. The abundant sp carbon chains, the efficient isomerization of the cumulenic content upon deposition suggest that polymerization is occurring during soot evolution [18]. It implies that either the local flame temperature favors a large amount of sp hybridized carbon instead of the polycyclic aromatic structure or growth by accretion of polyynic compounds is efficient. A large sp fraction is usually attained at higher temperature than in a typical flame (≈ 2000 ± 500K), according to atomistic simulations on carbon clusters [39,40,48]. Therefore, accretion of sp carbon chains and polymerization toward the polycyclic aromatic carbon skeleton is probably dominant but remains to be further investigated.

Acknowledgements

K.C.L. thanks the Vietnamese government for a doctoral scholarship and the European Union's Horizon 2020 research and innovation program under the Marie Skłodowska-Curie grant agreement [EU project 794156 – USFAOD] for her postdoctoral fellowship. The authors thank all the reviewers and in particular reviewer 4 for their careful reading of the manuscript and insightful comments and suggestions useful to improve it. We also thank our colleague, Andrew Mayne, helping to improve the language in the revision process.

Author Contributions

T.P. and K.C.L. conceptualized and designed the experiments. K.C.L. performed all experimental studies with support from C.L., and T.P. K.C.L and T.P. analyzed the results. K.C.L. and T.P. wrote the manuscript. All authors contributed to reading, discussion and commenting on the manuscript.

Author Information

The authors declare no competing financial interests.

Supplementary Materials:

Fig. S1

Scheme of online measurement of soot in the aerosol phase. In the inset, Flame 3.15 with the cone at HAB = 50 mm can be seen. The Raman spectrum of the soot on the computer screen is that at 50 mm in this Flame

Fig. S2

The excitation power density dependence of online spectra

Fig. S3

Comparison of various fitting options applied for online Raman spectra of aerosol soot produced at 22 mm.

Fig. S4

Curve fit with band combination for the first and the second orders of online Raman spectroscopy of soot produced by 3.15 Ethylene flame from HAB = 6 mm to HAB = 30 mm. The blue curves are the data, the red curves are the fitted spectra. Blue sky filled peaks are Raman finger print of ethylene redundant fuel.

Table S1

Fitting parameters of the first-order and second-order Raman bands

Note S1

Spectral fitting processes

Note S2

Assessment of uncertainty in this measurement

References and Notes

[1] J. Lelieveld, J.S. Evans, M. Fnais, D. Giannadaki, A. Pozzer, The contribution of outdoor air pollution sources to premature mortality on a global scale., Nature. 525 (2015) 367–371. doi:10.1038/nature15371.

[2] J. Zhou, K. Ito, R. Lall, M. Lippmann, G. Thurston, Time-series analysis of mortality effects of fine particulate matter components in Detroit and Seattle, Environ. Health Perspect. 119 (2011) 461–466. doi:10.1289/ehp.1002613.

[3] J.B. Howard, K.D. Chowdhury, J.B. Vander Sande, Carbon shells in flames, Nature. 370 (1994) 603.

[4] A. Goel, P. Hebgen, J.B. Vander Sande, J.B. Howard, Combustion synthesis of fullerenes and fullerenic nanostructures, Carbon 40 (2002) 177–182. doi:10.1016/S0008-6223(01)00170-1.

[5] N.K. Memon, S.D. Tse, J.F. Al-Sharab, H. Yamaguchi, A.M.B. Goncalves, B.H. Kear, Y. Jaluria, E.Y. Andrei, M. Chhowalla, Flame synthesis of graphene films in open

environments, Carbon 49 (2011) 5064–5070. doi:10.1016/j.carbon.2011.07.024.

[6] P. Minutolo, M. Commodo, A. Santamaria, G. De Falco, A. D'Anna, Characterization of flame-generated 2-D carbon nano-disks, Carbon 68 (2014) 138–148. doi:10.1016/j.carbon.2013.10.073.

[7] H.G. Wagner, Soot formation in combustion, Symp. (Int.) Combust. 17 (1979) 3–19. doi:10.1016/S0082-0784(79)80005-3.

[8] H.F. Calcote, Mechanisms of soot nucleation in flames-A critical review, Combust. Flame. 42 (1981) 215–242. doi:10.1016/0010-2180(81)90159-0.

[9] S.J. Harris, A.M. Weiner, Chemical Kinetics of Soot Particle Growth., Annu. Rev. Phys. Chem. 36 (1985) 31–52. doi:10.1146/annurev.physchem.36.1.31.

[10] P. Desgroux, X. Mercier, K.A. Thomson, Study of the formation of soot and its precursors in flames using optical diagnostics, Proc. Combust. Inst. 34 (2013) 1713–1738. doi:10.1016/j.proci.2012.09.004.

[11] M. Frenklach, D.W. Clary, W.C. Gardiner, S.E. Stein, Detailed kinetic modeling of soot formation in shock-tube pyrolysis of acetylene, Symp. (Int.) Combust. 20 (1985) 887–901. doi:10.1016/S0082-0784(85)80578-6.

[12] M. Frenklach, Reaction mechanism of soot formation in flames, Phys. Chem. Chem. Phys. 4 (2002) 2028–2037. doi:10.1039/b110045a.

[13] H. Bockhorn, Soot Formation in Combustion Mechanism and Models, Springer- Verlag Berlin, 1994.

[14] K.H. Homann, Fullerenes and soot formation - New pathways to large particles in flames, Angew. Chemie, Int. Ed. English. 37 (1998) 2435–2451. doi:10.1002/(SICI)1521-3773(19981002)37:18<2434::AID-ANIE2434>3.0.CO;2-L.

[15] H. Sabbah, L. Biennier, S.J. Klippenstein, I.R. Sims, B.R. Rowe, Exploring the Role of PAHs in the Formation of Soot: Pyrene Dimerization, J. Phys. Chem. Lett. 1 (2010) 2962–2967. doi:10.1021/jz101033t.

[16] H. Bladh, N.-E. Olofsson, T. Mouton, J. Simonsson, X. Mercier, A. Faccinetto, P.-E. Bengtsson, P. Desgroux, Probing the smallest soot particles in low-sooting premixed flames using laser-induced incandescence, Proc. Combust. Inst. 35 (2015) 1843–1850. doi:10.1016/j.proci.2014.06.001.

[17] F. Xu, P.B. Sunderland, G.M. Faeth, Soot formation in laminar premixed ethylene / air flames at atmospheric pressure, Combust. Flame. 108 (1997) 471–93. doi:10.1016/S0010-2180(96)00200-3.

[18] A. Ciajolo, Condensed phases in soot formation process, in: H. Bockhorn, A. D'Anna, A.F.

Sarofim, H. Wang (Eds.), Combustion Generated Fine Carbonaceous Particles, KIT scientific publishing, Karlsruhe, 2009: pp. 333–344.

[19] K.O. Johansson, M.P. Head-Gordon, P.E. Schrader, K.R. Wilson, H.A. Michelsen, Resonance-stabilized hydrocarbon-radical chain reactions may explain soot inception and growth, Science 361 (2018) 997–1000. doi:10.1126/science.aat3417.

[20] H.A. Michelsen, Probing soot formation, chemical and physical evolution, and oxidation: A review of in situ diagnostic techniques and needs, Proc. Combust. Inst. 36 (2017) 717–735. doi:10.1016/j.proci.2016.08.027.

[21] A. Milani, M. Tommasini, V. Russo, A.L. Bassi, A. Lucotti, F. Cataldo, C.S. Casari, Raman spectroscopy as a tool to invertigate the structure and electronic properties of carbon-atom wires, Beilstein J. Nanotechnol. 6 (2015) 480–491. doi:10.3762/bjnano.6.49.

[22] A. Sadezky, H. Muckenhuber, H. Grothe, R. Niessner, U. Pöschl, Raman microspectroscopy of soot and related carbonaceous materials: Spectral analysis and structural information, Carbon 43 (2005) 1731–1742. doi:10.1016/j.carbon.2005.02.018.

[23] N. Larouche, B.L. Stansfield, Classifying nanostructured carbons using graphitic indices derived from Raman spectra, Carbon 48 (2010) 620–629. doi:10.1016/j.carbon.2009.10.002.

[24] A. Ferrari, J. Robertson, Interpretation of Raman spectra of disordered and amorphous carbon, Phys. Rev. B. 61 (2000) 14095–14107. doi:10.1103/PhysRevB.61.14095.

[25] K.C. Le, C. Lefumeux, P.-E. Bengtsson, T. Pino, Direct observation of aliphatic structures in soot particles produced in low-pressure premixed ethylene flames via online Raman spectroscopy, Proc. Combust. Inst. 37 (2019) 869–876. doi:10.1016/j.proci.2018.08.003.

[26] R. Brunetto, T. Pino, E. Dartois, A.T. Cao, L. D'Hendecourt, G. Strazzulla, P. Bréchignac, Comparison of the Raman spectra of ion irradiated soot and collected extraterrestrial carbon, Icarus. 200 (2009) 323–337. doi:10.1016/j.icarus.2008.11.004.

[27] C. Russo, A. Ciajolo, Effect of the flame environment on soot nanostructure inferred by Raman spectroscopy at different excitation wavelengths, Combust. Flame. 162 (2015) 2431–2441. doi:10.1016/j.combustflame.2015.02.011.

[28] M. Saffaripour, L.L. Tay, K.A. Thomson, G.J. Smallwood, B.T. Brem, L. Durdina, M. Johnson, Raman spectroscopy and TEM characterization of solid particulate matter emitted from soot generators and aircraft turbine engines, Aerosol Sci. Technol. 51 (2017) 518–531. doi:10.1080/02786826.2016.1274368.

[29] S. Dasappa, J. Camacho, Evolution in size and structural order for incipient soot formed at flame temperatures greater than 2100 K, Fuel. 291 (2021) 120196. doi:10.1016/j.fuel.2021.120196.

[30] L. Gavilan, K.C. Le, T. Pino, I. Alata, A. Giuliani, E. Dartois, Polyaromatic amorphous carbons as carriers of the UV bump : FUV to mid-infrared spectroscopy of laboratory analogs, Astron. Astrophys. 607 (2017). doi:10.1051/0004-6361/201730712.

[31] P. Desgroux, A. Faccinetto, X. Mercier, T. Mouton, D. Aubagnac Karkar, A. El Bakali, Comparative study of the soot formation process in a “nucleation” and a “sooting” low pressure premixed methane flame, Combust. Flame. 184 (2017) 153–166. doi:10.1016/j.combustflame.2017.05.034.

[32] K.C. Le, J. Henriksson, P.E. Bengtsson, Polarization effects in Raman spectroscopy of light-absorbing carbon, Raman Spectrosc. 52 (2021) 1115–1122. doi:10.1002/jrs.6107.

[33] K.C. Le, T. Pino, V.T. Pham, J. Henriksson, S. Török, P.-E. Bengtsson, Raman spectroscopy of mini-CAST soot with various fractions of organic compounds: Structural characterization during heating treatment from 25 °C to 1000 °C, Combust. Flame. 209 (2019) 291–302. doi:10.1016/J.COMBUSTFLAME.2019.07.037.

[34] L. Mueller, G. Jakobi, J. Orasche, E. Karg, M. Sklorz, G. Abbaszade, B. Weggler, L. Jing, J. Schnelle-Kreis, R. Zimmermann, Online determination of polycyclic aromatic hydrocarbon formation from a flame soot generator Aerosols and Health, Anal. Bioanal. Chem. 407 (2015) 5911–5922. doi:10.1007/s00216-015-8549-x.

[35] S. Bejaoui, X. Mercier, P. Desgroux, E. Therssen, Laser induced fluorescence spectroscopy of aromatic species produced in atmospheric sooting flames using UV and visible excitation wavelengths, Combust. Flame. 161 (2014) 2479–2491. doi:10.1016/j.combustflame.2014.03.014.

[36] G. Magnotti, K.C. Utsav, P.L. Varghese, R.S. Barlow, Raman spectra of methane, ethylene, ethane, dimethyl ether, formaldehyde and propane for combustion applications, J. Quant. Spectrosc. Radiat. Transf. 163 (2015) 80–101. doi:10.1016/j.jqsrt.2015.04.018.

[37] A.C. Ferrari, J. Robertson, Resonant Raman spectroscopy of disordered, amorphous, and diamondlike carbon, Phys. Rev. B. 64 (2001) 075414. doi:10.1103/PhysRevB.64.075414.

[38] B. Dippel, H. Jander, J. Heintzenberg, NIR FT Raman spectroscopic study of flame soot, Phys. Chem. Chem. Phys. 1 (1999) 4707–4712. doi:10.1039/a904529e.

[39] F. Cataldo, The role of Raman spectroscopy in the research on sp-hybridized carbon chains: Carbynoid structures polyynes and metal polyynides, J. Raman Spectrosc. 39 (2008) 169–176. doi:10.1002/jrs.1830.

[40] L. Ravagnan, T. Mazza, G. Bongiorno, M. Devetta, M. Amati, P. Milani, P. Piseri, M. Coreno, C. Lenardi, F. Evangelista, P. Rudolf, sp hybridization in free carbon nanoparticles-presence and stability observed by near edge X-ray absorption fine structure spectroscopy.,

Chem. Commun. 47 (2011) 2952–4. doi:10.1039/c0cc03778h.

[41] K.O. Johansson, T. Dillstrom, M. Monti, F. El Gabaly, M.F. Campbell, P.E. Schrader, D.M. Popolan-Vaida, N.K. Richards-Henderson, K.R. Wilson, A. Violi, H.A. Michelsen, Formation and emission of large furans and oxygenated hydrocarbons from flames, Proc. Natl. Acad. Sci. 113 (2016) 8374–8379. doi:10.1073/pnas.1604772113.

[42] Y. Liu, C. Liu, J. Ma, Q. Ma, H. He, Structural and hygroscopic changes of soot during heterogeneous reaction with O3, Phys. Chem. Chem. Phys. 12 (2010) 10896–10903. doi:10.1039/c0cp00402b.

[43] C. Casari, A. Li Bassi, L. Ravagnan, F. Siviero, C. Lenardi, P. Piseri, G. Bongiorno, C. Bottani, P. Milani, Chemical and thermal stability of carbyne-like structures in cluster-assembled carbon films, Phys. Rev. B. 69 (2004) 075422. doi:10.1103/PhysRevB.69.075422.

[44] L. Ravagnan, F. Siviero, C. Lenardi, P. Piseri, E. Barborini, P. Milani, C.S. Casari, A. Li Bassi, C.E. Bottani, Cluster-Beam Deposition and in situ Characterization of Carbyne-Rich Carbon Films, Phys. Rev. Lett. 89 (2002) 285506. doi:10.1103/PhysRevLett.89.285506.

[45] K.C. Le, Raman spectroscopy of soot produced in low pressure flames: ex-situ analyses and online gas phase studies, Paris Saclay, 2017. doi:10.13140/RG.2.2.35396.27524.

[46] T. K. C. Le; B. Héraud; C. Lefumeux; T. Pino, On the polarization dependence of Raman scattering of soot nanoparticles in the gas phase, 9th International Conference Optical Photonics (2017), page 88–92.

[47] L. Ravagnan, G. Bongiorno, D. Bandiera, E. Salis, P. Piseri, P. Milani, C. Lenardi, M. Coreno, M. de Simone, K.C. Prince, Quantitative evaluation of sp/sp^2 hybridization ratio in cluster-assembled carbon films by in situ near edge X-ray absorption fine structure spectroscopy, Carbon 44 (2006) 1518–1524. doi:10.1016/j.carbon.2005.12.015.

[48] S. Farris, S. Pozzoli, P. Biagioni, L. Duó, S. Mancinelli, L. Piergiovanni, The fundamentals of flame treatment for the surface activation of polyolefin polymers - A review, Polymer. 51 (2010) 3591–3605. doi:10.1016/j.polymer.2010.05.036.

[49] F. Negri, C. Castiglioni, M. Tommasini, G. Zerbi, A computational study of the Raman spectra of large polycyclic aromatic hydrocarbons: Toward molecularly defined subunits of graphite, J. Phys. Chem. A. 106 (2002) 3306–3317. doi:10.1021/jp0128473.

[50] A.C. Ferrari, J.C. Meyer, V. Scardaci, C. Casiraghi, M. Lazzeri, F. Mauri, S. Piscanec, D. Jiang, K.S. Novoselov, S. Roth, A.K. Geim, Raman spectrum of graphene and graphene layers, Phys. Rev. Lett. 97 (2006) 1–4. doi:10.1103/PhysRevLett.97.187401.

[51] C. Castiglioni, C. Mapelli, F. Negri, G. Zerbi, Origin of the D line in the Raman spectrum of graphite: A study based on Raman frequencies and intensities of polycyclic aromatic

hydrocarbon molecules, J. Chem. Phys. 114 (2001) 963–974. doi:10.1063/1.1329670.

[52] H.A. Michelsen, M.B. Colket, P.E. Bengtsson, A. D'Anna, P. Desgroux, B.S. Haynes, J.H. Miller, G.J. Nathan, H. Pitsch, H. Wang, A review of terminology used to describe soot formation and evolution under combustion and pyrolytic conditions, ACS Nano. 14 (2020) 12470–12490. doi:10.1021/acsnano.0c06226.

[53] B. Apicella, A. Tregrossi, J. Abrahamson, R.L. Vander Wal, C. Russo, The effect of temperature on soot properties in premixed ethylene flames, Combust. Sci. Technol. 191 (2019) 1558–1570. doi:https://doi.org/10.1080/00102202.2019.1566228.

[54] J. Bonpua, Y. Yagües, A. Aleshin, S. Dasappa, J. Camacho, Flame temperature effect on sp2 bonds on nascent carbon nanoparticles formed in premixed flames ($T_{f,max}$ > 2100 K): A Raman spectroscopy and particle mobility sizing study, Proc. Combust. Inst. 37 (2019) 943–951. doi:10.1016/j.proci.2018.06.124.

[55] A. Faccinetto, C. Irimiea, P. Minutolo, M. Commodo, N. Nuns, Y. Carpentier, C. Pirim, P. Desgroux, C. Focsa, A.D. Anna, X. Mercier, Evidence on the formation of dimers of polycyclic aromatic hydrocarbons in a laminar diffusion flame, Commun. Chem. 3 (2020) 1–8. doi:10.1038/s42004-020-00357-2.

[56] X. Mercier, A. Faccinetto, S. Batut, G. Vanhove, Selective identification of cyclopentaring-fused PAHs and side-substituted PAHs in a low pressure premixed sooting flame by photoelectron photoion coincidence spectroscopy, 22 (2020) 15926–15944. doi:10.1039/d0cp02740e.

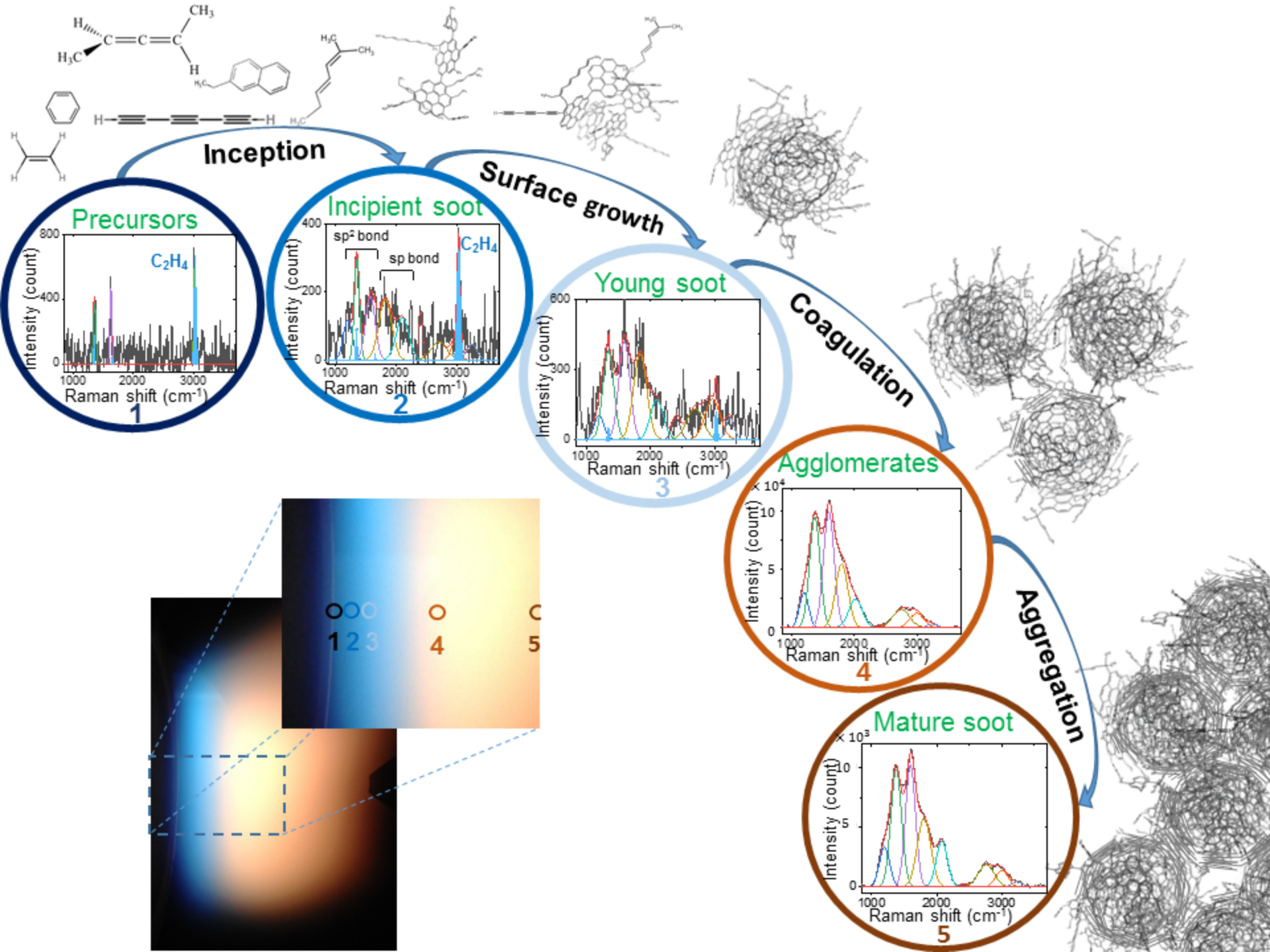
Inception
Surface growth
Coagulation
Aggregation
Precursors
C_2H_4
Intensity (count)
Raman shift (cm^{-1})
1
Incipient soot
sp^2 bond
sp bond
C_2H_4
Intensity (count)
Raman shift (cm^{-1})
2
Young soot
Intensity (count)
Raman shift (cm^{-1})
3
Agglomerates
Intensity (count)
Raman shift (cm^{-1})
4
Mature soot
Intensity (count)
Raman shift (cm^{-1})
5
1 2 3
4
5